JOM, Vol. 71, No. 11, 2019
https://doi.org/10.1007/s11837-019-03498-5

Thermal and Electrical Properties of Highly Dense Ceramic Materials Based on Co-doped $LaYO_3$

A. KASYANOVA,[1,2,3] L. TARUTINA,[1,2] J. LYAGAEVA,[1,2] G. VDOVIN,[1] D. MEDVEDEV,[1,2,4] and A. DEMIN[1,2]

1.—Institute of High Temperature Electrochemistry, Yekaterinburg, Russia 620137. 2.—Ural Federal University, Yekaterinburg, Russia 620002. 3.—e-mail: kasyanova.1996@list.ru. 4.—e-mail: dmitrymedv@mail.ru

Solid oxide electrolytes showing proton transport are extensively studied materials, which can be utilised in different types of highly efficient energy systems such as solid oxide fuel cells, solid oxide electrolysis cells, membrane converters and sensors. Here we present the results of a study of the functional properties of $LaYO_3$-based materials, which exhibit higher chemical stability than the more well known proton-conducting electrolytes, cerates and zirconates of alkaline earth elements. The structural, ceramic, thermal and electrical properties of $La_{0.9}Sr_{0.1}YO_{3-\delta}$ have been thoroughly studied depending on the partial Y substitution with some lanthanides (10 mol.% of Yb, Dy, Ho). According to the experimental data, $La_{0.9}Sr_{0.1}Y_{0.9}Yb_{0.1}O_{3-\delta}$ can be considered a promising alternative to the basic oxide because of its better transport properties and the fact that there are no detrimental changes in other functional characteristics.

INTRODUCTION

High-temperature protonic conductors (HTPCs) form a class of materials that enable the demonstration of proton transportation along with oxygen-ionic and electronic (*p*-type) transportation.[1,2] Due to the very high mobility of proton charge carriers coupled with low activation energy, high proton conductivity levels might be reached for an intermediate-temperature range (400–800°C) and could surpass the oxygen ionic conductivity values under the same conditions.[3,4] These characteristics show promise for HTPC application in a wide range of solid oxide electrochemical devices, such as fuel cells,[5,6] sensors,[7–10] pumps,[11,12] electrolysis cells[13,14] and membrane reactors.[15,16]

Proton transport has been revealed for different systems, such as barium cerates and zirconates, lanthanum orthoniobates and scandates, etc.[2,17] One of the most studied HTPCs is material based on barium cerate and zirconate because of high proton conductivity.[18,19] However, $BaCeO_3$- and $BaZrO_3$-based oxides suffer from insufficient chemical stability in the presence of CO_2 and H_2O because of gradual carbonate/hydroxide formation.[20] Another key problem is the high sintering temperatures required for preparing highly dense ceramic materials.[21]

There are a number of possible ways to resolve the aforementioned issues. For example, the phase stability of barium cerate can be enhanced by doping[22] (In^{3+}, Nb^{5+}, Sn^{4+}, Ca^{2+}); the design of new materials with a low Ba concentration (for example, $LaNbO_4$, $La_2Ce_2O_7$, $LaYO_3$) is also an alternative way to develop chemically stable oxides.[23–26] Lanthanum yttrate ($LaYO_3$) represents the perovskite structure HTPC family. Doped $LaYO_3$-based materials have high chemical stability in the presence of H_2O/CO_2 due to the absence of barium cations causing the subsequent formation of impurity phases with barium.[27] Moreover, the yttrates exhibit a wide electrolytic domain boundary and no phase transitions between 20°C and 1400°C,[28] representing some technological advantages from the thermomechanical point of view. Since the ionic conductivity of these materials is lower than those of $BaCeO_3$ or $BaZrO_3$, the application of yttrates is unlikely to be practical under real conditions. Nevertheless, they can be effectively used in electrochemical solid-state gas sensors[29]

(Published online May 7, 2019)

when the operation of such analytical devices is not affected by the ohmic resistance of electrolytes. However, a limited range of $LaYO_3$-based derivatives has been characterised. Traditionally, $LaYO_3$ has been modified by carrying out A-site doping with alkaline earth elements as acceptor dopants,[27,28] while the effect of B-site substitution of $LaYO_3$ on the functional properties has been considered to a lesser extent.[29,30]

In this work, one of the most studied yttrates ($La_{0.9}Sr_{0.1}YO_{3-\delta}$) was selected as a model oxide and its doping with M_2O_3 (M = Yb, Ho, Dy) was performed to evaluate the effect of such an isovalent doping on the structural, thermal and electrical properties of the $La_{0.9}Sr_{0.1}Y_{0.9}M_{0.1}O_{3-\delta}$ materials. Special attention was paid to the fabrication of the single-phase and highly dense ceramic materials, which, according to analysis of literature data, is one of the greatest technological challenges.

EXPERIMENTAL PROCEDURES

Materials Synthesis

The $La_{0.9}Sr_{0.1}Y_{0.9}M_{0.1}O_{3-\delta}$ (M = Y, Yb, Dy, Ho) materials were synthesised via a citrate–nitrate synthesis method, which included the decomposition of organometallic complexes at high temperatures. $SrCO_3$, $La(NO_3)_3{\cdot}6H_2O$, $Y(NO_3)_3{\cdot}6H_2O$, Yb_2O_3, Ho_2O_3 and Dy_2O_3 with a purity higher than 99.0% were used as starting reagents. Strontium carbonate and oxides were first calcined at 200°C (2 h) and 1000°C (2 h), respectively, taken in stoichiometric amounts and then dissolved in a diluted solution of nitric acid. Citric acid as a complexing agent and fuel was added in an equimolar amount relative to the total moles of cations. The resulting solution was slowly heated to 100°C under stirring. After that, an ammonia solution was added to obtain the neutral condition (pH ≈ 7). The final solution was heated up to 300°C to initiate the processes of active water evaporation and, subsequently, residue self-ignition. Preliminary heat treatment of the obtained disperse powders was carried out at 1050°C for 5 h. Following subsequent mechanical activation of the powders, they were synthesised at 1100°C for 5 h.

The cylindrical pellets were prepared by uniaxial pressing of the powders followed by their sintering at 1450°C for 5 h. The behaviour of the ceramic samples under sintering was estimated using the data on total shrinkage and relative density.

Structural and Microstructural Characterisation

The phase structure of the sintered materials was studied by X-ray diffraction (XRD) analysis using a DMAX-2500 diffractometer with Ni-filtered CuKα radiation.[31] The data were obtained at room temperature in a 2θ range of 20°–80° and a scanning step of 0.02°. The structural parameter refinement was performed by the Rietveld method using Fullprof software.[32]

The morphology of the ceramic samples was analysed by means of a TESCAN MIRA 3 LMU scanning electron microscope.[31]

Thermal and Electrical Characterisation

Thermal behaviour of the materials was studied with a DIL 402 C dilatometer between 25°C and 1000°C in air atmosphere. The heating/cooling rate was equal to 5°C min^{-1}. The obtained data were used to determine the thermal expansion coefficients (TECs).

Electrical properties were studied using both two-probe AC and four-probe DC methods. The former was used to separate the total conductivity on bulk and grain boundary components, while the latter to evaluate the high-temperature transport.

The low-temperature data (200–600°C) were obtained using the electrochemical impedance spectroscopy (EIS) technique. The cylindrical samples were thoroughly polished before an Ag-based slurry (Ag/Ag_2O powders in an organic binder) was formed on both their surfaces. The electrodes were formed after a sintering procedure (800°C for 1 h). Electroactivation of the electrodes [infiltration with a $Pr(NO_3)_3$-containing solution and calcination at 600°C] was carried out prior to electrochemical measurements. The impedance spectra were obtained using a FRA MaterialsM 520 associated with a potentiostat/galvanostat Amel 2550 and analysed using Zview software.

The high-temperature data were obtained on a bar-shaped sample with the highest conductivity in the temperature range of 500–900°C in wet (3%) air atmosphere as well as within the oxygen partial pressure range of 10^{-18}–0.21 atm. at 700, 800 and 900°C.

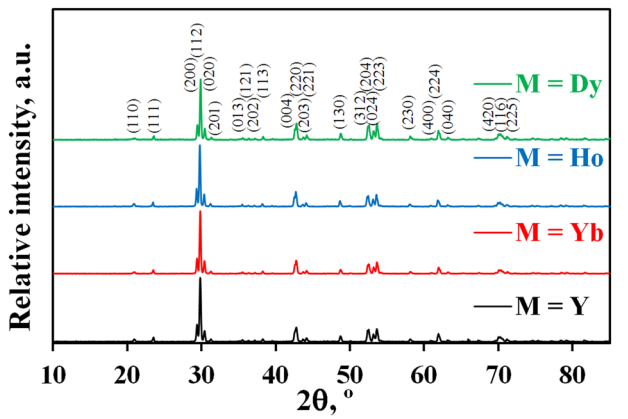

Fig. 1. XRD patterns of the $La_{0.9}Sr_{0.1}Y_{0.9}M_{0.1}O_{3-\delta}$ ceramic samples sintered at 1450°C.

Table I. Refined lattice parameters of $La_{0.9}Sr_{0.1}Y_{0.9}M_{0.1}O_{3-\delta}$ sintered at 1450°C

M	r^{VI} (Å/Snannon[22])	a (Å)	b (Å)	c (Å)	V (Å^3)
Yb	0.868	6.073	8.483	5.878	302.84
Y	0.893	6.067	8.493	5.883	303.18
Ho	0.901	6.081	8.501	5.883	304.12
Dy	0.912	6.083	8.503	5.888	304.51

Table II. Total shrinkage (L), relative density (ρ) and grain size characteristics (D_{10}, D_{50} and D_{90}) of the sintered $La_{0.9}Sr_{0.1}Y_{0.9}M_{0.1}O_{3-\delta}$ materials

M	L (%)	ρ (%)	D_{10} (μm)	D_{50} (μm)	D_{90} (μm)
Yb	18.6	96.1	0.6	1.4	2.5
Y	18.3	95.7	0.7	1.6	2.6
Ho	18.3	97.1	0.9	1.8	3.3
Dy	18.9	95.5	0.7	1.9	3.1

RESULTS AND DISCUSSION

Phase Structure

According to the XRD results (Fig. 1), all the sintered ceramic materials are single-phase and crystallise in a perovskite structure. The XRD patterns consist of the same combination of reflexes, number and form, none of which change with doping; this implies that both basic (undoped) and doped samples have the same symmetry (orthorhombic structure, Pna21 space group). Table I lists the results of the Rietveld refinement (see example in Fig. S1). As can be seen, the lattice parameters tend to increase from M = Yb to M = Dy, which directly indicates that the expansion of the cells is determined by higher ionic radii of the introduced dopants.

Microstructural Properties

The total shrinkage of all the sintered samples is found to be around 18%, while the relative density (calculated as a ratio of the measured and theoretical densities, i.e., about 8.1 g cm^{-3}) exceeds 95% (Table II). These parameters indicate that the yttrates are characterised by excellent densification behaviour.

SEM analysis (Fig. 2) shows that the morphology of the samples is quite dense, consists of well-connected grains and does not present any visible micro-sized pores. The SEM images were used to determine the mean grain size (D_{mean}). In detail, the size of about 100 grains was determined by the Get Data Graph Digitizer software[33] and then statistically analysed (Fig. S2). According to the performed analysis, the Yb-containing yttrate has the lowest D_{mean}, which increases with increasing ionic radii of M^{3+} (Table II). This result can be explained by the fact that the dopants with high ionic radii result in the formation of crystal structures with high lattice parameters. Due to their large basis, the M–O bonds are lengthened with simultaneous deterioration of their strength. As a result, this accelerates the diffusion process while using high (sintering) temperatures.

It should be noted that the fabrication of the single-phase and highly dense $LaYO_3$-based ceramic materials is an extremely difficult task. On the one hand, it is associated with a low range of solid solution existence; on the other hand, with difficulties in preparing the well-densified materials. For example, only a limited number of published works present the microstructural data of yttrates, which, however, show either the formation of porous samples[29,34] or multi-phase ceramics.[35] Therefore, the utilisation of the proposed citrate–nitrate technique allows both of these problems to be solved by means of excellent homogeneous powder products in a sub-micron state.

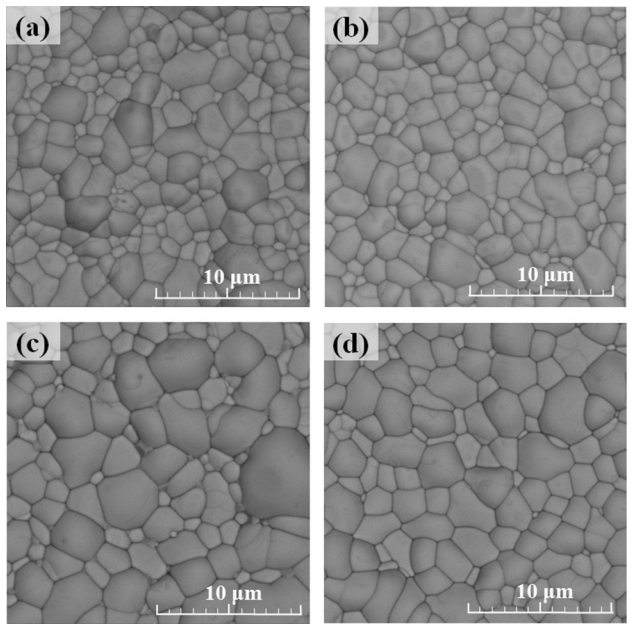

Fig. 2. Morphology of the sintered $La_{0.9}Sr_{0.1}Y_{0.9}M_{0.1}O_{3-\delta}$ ceramic materials in back-scattered electron imaging mode: M = Yb (a), M = Y (b), M = Ho (c) and M = Dy (d).

Thermal Properties

Figure 3 presents the temperature dependencies of relative dimension changes in the ceramic samples and cooling mode. All the samples demonstrate a linear behaviour in the dilatometric curve in a range of 100–1000°C, without any visible bending, implying the absence of phase transition(s) and effects associated with substantial chemical strain.

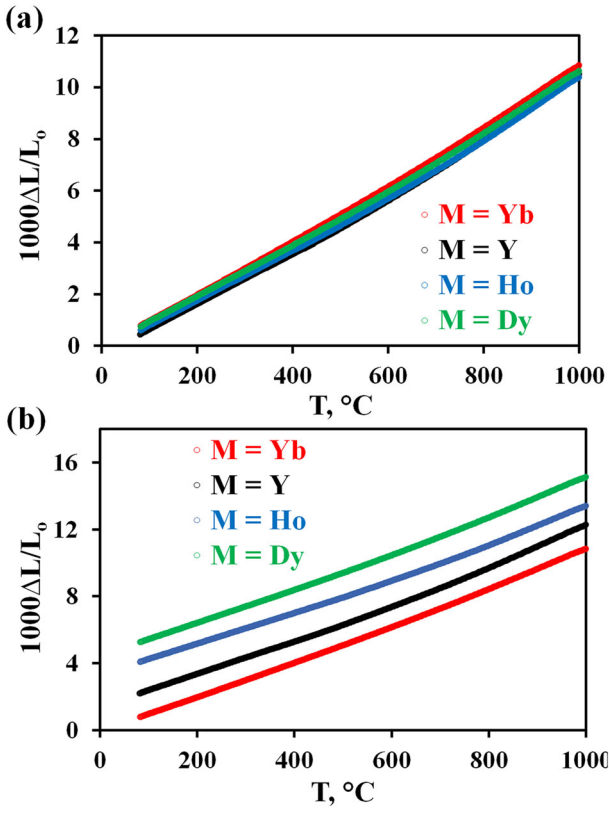

Fig. 3. Dilatometric curves for the $La_{0.9}Sr_{0.1}Y_{0.9}M_{0.1}O_3$ ceramic samples under cooling mode: original data (a) and displacement curves (b).

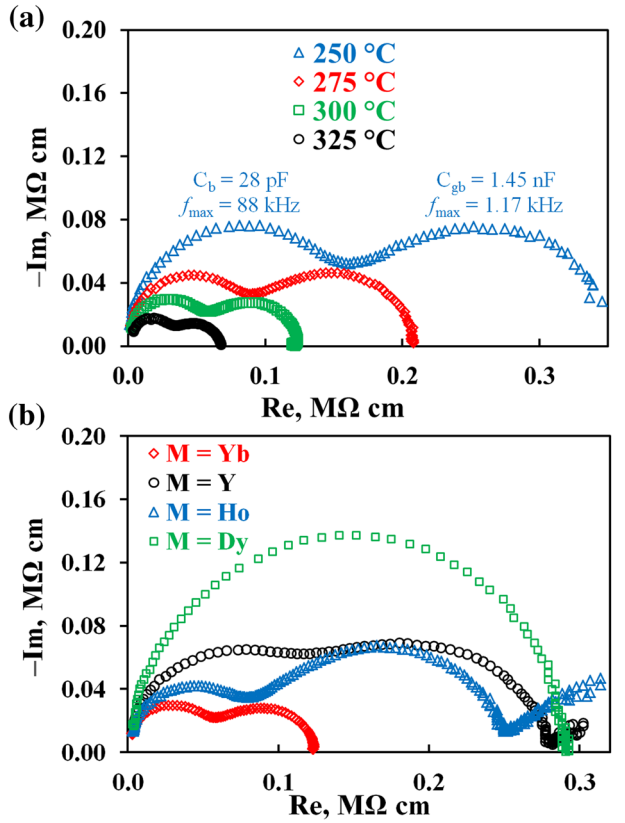

Fig. 4. Examples of impedance spectra fitting for $La_{0.9}Sr_{0.1}Y_{0.9}Yb_{0.1}O_3$ with the separation total conductivity onto bulk and grain boundary contributions at different temperatures (a) and impedance spectra for all samples at 300°C (b).

According to Mizuno et al.,[36] Coutures et al.[37] and Gorelov et al.,[38] an orthorhombic/monoclinic phase transition of the $LaYO_3$ materials occurs around 1450°C. For A- and B- co-doped perovskites of this family, such a transition is proposed to be realised at higher temperatures, since the ceramic samples sintered at 1450°C were indexed in the frame of the orthorhombic-distorted structure. The TEC values of $La_{0.9}Sr_{0.1}Y_{0.9}M_{0.1}O_{3-\delta}$ are virtually identical: $(10.7 \pm 0.5)\ 10^{-6}\ K^{-1}$ under heating and $(10.6 \pm 0.6)\cdot 10^{-6}\ K^{-1}$ under cooling. No meaningful changes in TECs can be associated with a low substitution degree of the basic yttrium cations with other lanthanides.

Electrical Properties

If thermal behaviour is a weakly sensitive characteristic, the transport could change more considerably, even with slight doping. Regularities in bulk ($R_{b.}$) and grain boundary ($R_{g.b.}$) resistance variations are shown in Fig. 4. At least one or two semicircles can be distinguished in the spectra, which correspond to $R_{b.}$ and $R_{g.b.}$ components. The size of these semicircles decreases with increasing temperature; at the same time, they merge into one semicircle at higher temperatures, which complicates the analysis and separation of the two resistance components. The data obtained were analysed according to the general equivalent circuit scheme, $R_b.Q_b - R_{g.b.}Q_{g.b.} - R_pQ_p$. Here, R_p is the polarisation resistance of the electrodes and Q is the constant phase element of the corresponding processes.

The values of the frequency (f_{max}) and capacitance (C) characteristics were determined according to Eqs. 1 and 2 to confirm the adequacy of the selected model.

$$C = (R \cdot Q)^{1/n} \cdot R^{-1} \quad (1)$$

$$f_{max} = (R \cdot Q)^{-1/n} \cdot (2\pi)^{-1} \quad (2)$$

According to the capacitance values, the first arc is indeed related to the bulk characteristics, while the second arc highlights the grain boundary transport. It is interesting to note that only the bulk process (with capacitance values of ~ 22 pF) is observed for the Dy-doped yttrate (Fig. 4b), which might be associated with a lower grain boundary resistance as a result of the lowest specific grain boundary density or the highest grain size (Table II).

Figure 5 displays the temperature dependencies of bulk, grain boundary and total conductivities in

Arrhenius coordinates. As can be seen, the M-doping of $La_{0.9}Sr_{0.1}YO_{3-\delta}$ slightly affects the bulk components (Fig. 5a), except in the Dy-doped sample having the bulk conductivity, which is ~ 4 times lower than those for the basic sample and other doped analogues. This result can be explained using the term derived from Goldschmidt's tolerance factor:[39,40]

$$t = \frac{r_A + r_O}{\sqrt{2}(r_B + r_O)} \quad (3)$$

Here, r_A, r_B and r_O are the average ionic radii of A, B and O ions in ABO_3-based oxides. According to this formula, an increase in the average B radius results in a decrease of the t values accompanied by a distortion of the perovskite structure. For example, $LaDyO_3$ and $LaGdO_3$ have a monoclinic-type perovskite structure[40–42] instead of the orthorhombic-type one for $LaYO_3$. The high degree of such a distortion impedes the dynamic mobility of ions because of structural peculiarities, in particular creating a one-dimensional pathway for proton transportation.[43] From the other side, the transport behaviour of the $LaMO_3$ perovskites changes from protonic for M = Y and Yb to predominantly oxygen-ionic for the B-site cations with very low ionic radii, M = Ga. In detail, $LaGaO_3$-based oxides represent well-known oxygen-conducting electrolytes,[44,45] while $LaScO_3$-based oxides (r_{Sc} is between r_{Ga} and r_Y) exhibit co-ionic (oxygen-ionic and protonic) transport.[46,47]

Regarding the grain boundary conductivity (Fig. 5b), the Yb-doped ceramic material demonstrates the maximal values among the basic and Ho-containing samples, although the former exhibits a higher grain boundary density (Fig. S3). These results also support the above-mentioned proposal, when factors related to the crystal structure have a stronger impact on the grain boundary transport properties than microstructural factors.

A correlation of total conductivities under relatively low measurement temperatures (Fig. 5c)

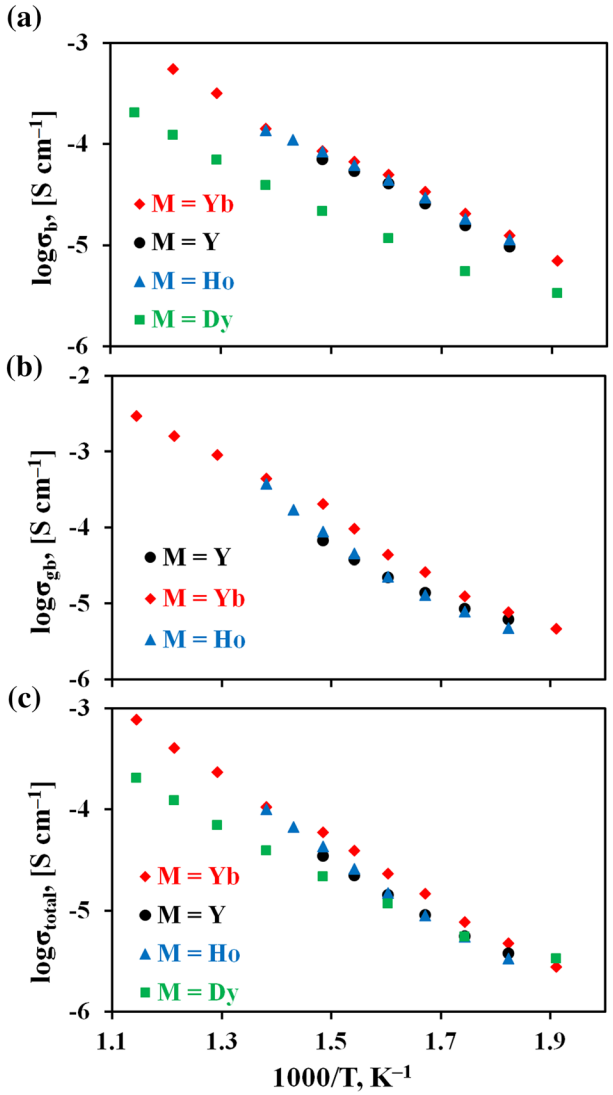

Fig. 5. Temperature dependences of bulk (a), grain boundary (b), total (c) conductivities for the $La_{0.9}Sr_{0.1}Y_{0.9}M_{0.1}O_{3-\delta}$ samples in wet air atmosphere.

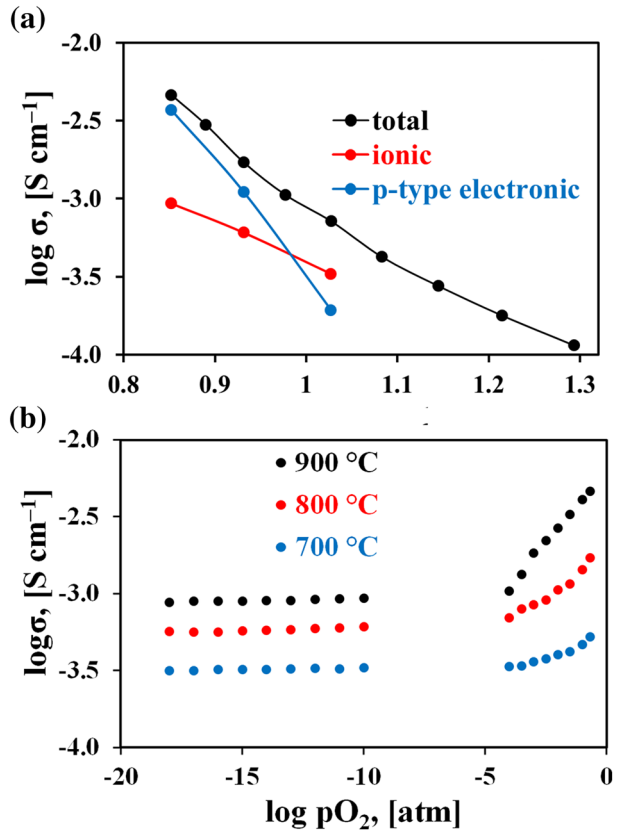

Fig. 6. Temperature dependences of total conductivity of the $La_{0.9}Sr_{0.1}Y_{0.9}Yb_{0.1}O_{3-\delta}$ sample in wet air atmosphere and its ionic and electronic contributions (a) determined on the base of the total conductivity depending on the oxygen partial pressure level (b).

reveals a similar character for bulk and grain boundary properties, when Yb- and Dy-containing samples exhibit the highest and lowest conductivity levels, respectively. For the former sample, the total conductivity has been determined over the high-temperature range depending on the temperature or oxygen partial pressure variation (Fig. 6). Regarding the temperature factor, the total conductivity of the $La_{0.9}Sr_{0.1}Y_{0.9}Yb_{0.1}O_{3-\delta}$ ceramic sample increases from 0.1 to 4.6 mS cm^{-1} at 500 and 900°C, respectively, with an activation energy of ~ 0.77 eV. This conductivity at high temperatures (> 600°C) consists of the ionic and electronic conductivities with the corresponding activation energies of 0.57 and 1.62 eV (Fig. 6a). Separation of the total conductivity on the partial components is performed by measuring the electrical properties that depend on pO_2 variation (Fig. 6b), since the p-type electronic conductivity (σ_p), in contrast to ionic (σ_{ion}), is sensitive to such a variation:[48,49]

$$\sigma = \sigma_{ion} + \sigma_p = \sigma_{ion} + \sigma_{p,o}(pO_2)^{1/4} \quad (4)$$

The analysis was performed at relatively high temperatures (700°C, 800°C, and 900°C), within which the total conductivity changed noticeably in the high pO_2 range, enabling the proposed separation to be carried out.

As can be seen in Fig. 6a, the activation energy of ionic conductivity is quite low, which is a characteristic feature of proton transport.[50,51] Therefore, it can be concluded that proton conductivity predominates over the oxygen-ionic one even under a low water vapour partial pressure (pH_2O = 0.03 atm.), which is in line with the data of Okuyama et al.[22,28] From this viewpoint, $LaYO_3$ comprises a basis for promising proton conductors with an advantage over other examples of this class due to a high contribution of proton conductivity, even at high temperatures. Moreover, the level of proton conductivity of the doped yttrates (0.32 mS cm^{-1} at 700°C) exceeds those of other La-based proton conductors, for example, 0.04 mS cm^{-1} for $La_2Ce_2O_7$,[52] 0.03 mS cm^{-1} for Ca-doped $La_2Zr_2O_7$[53] and 0.01 mS cm^{-1} for Ba-doped $LaNb_3O_{9-\delta}$[23] at the same temperature.

CONCLUSION

In the present work, the $La_{0.9}Sr_{0.1}Y_{0.9}M_{0.1}O_{3-\delta}$ materials (M = Yb, Y, Ho, Dy) were successfully synthesised using the citrate–nitrate combustion route and highly dense ceramic samples were prepared at a relatively low sintering temperature (1450°C). The slight doping of yttrium with other lanthanides results in changes in lattice constants in agreement with their ionic radii, while the perovskite symmetry (orthorhombic singony, sp. gr. Pna21) remains unchanged. All the samples are well densified; they have a relative density of 95% or higher with no evidence of visible pores. According to the dilatometry results, the doped materials as well as the basic one exhibited a similar thermal expansion behaviour with virtually the same average thermal expansion values $(10.6 \pm 0.6)\cdot10^{-6}$ K^{-1}. The most visible changes were observed in transport properties, which showed that the highest grain and grain boundary conductivities were reached for the $La_{0.9}Sr_{0.1}Y_{0.9}Yb_{0.1}O_{3-\delta}$ ceramic material. Such an improvement was associated with a decrease in the distortion of the perovskite structure, favourable for ion transportation. The results of high-temperature conductivity measurements for the Yb-containing composition revealed that its ionic conductivity was determined by the protonic transport because of a relatively low activation energy level (below 0.6 eV). It can be noted that Sr and Yb co-doped $LaYO_3$ can be considered representative of proton-conducting electrolytes with a good combination of transport properties and stability caused by the absence (or reduced amount) of alkaline-earth elements, especially barium.

ACKNOWLEDGEMENTS

This work was performed according to the budgetary plans of the Institute of High Temperature Electrochemistry. Dr. Dmitry Medvedev is also grateful to the Council of the President of the Russian Federation (scholarship СП-161.2018.1). The characterisation of powder and ceramic materials was carried out at the Shared Access Centre "Composition of Compounds" of the Institute of High Temperature Electrochemistry.

ELECTRONIC SUPPLEMENTARY MATERIAL

The online version of this article (https://doi.org/10.1007/s11837-019-03498-5) contains supplementary material, which is available to authorized users.

REFERENCES

1. E.C.C. Souza and R. Muccillo, *J. Mater. Res.* 13, 3 (2010).
2. R. Haugsrud, *Diff. Found.* 8, 31 (2016).
3. N. Kochetova, I. Animitsa, D. Medvedev, A. Demin, and P. Tsiakaras, *RSC Adv.* 6, 73222 (2016).
4. S. Hossain, A.M. Abdalla, S.N.B. Jamain, J.H. Zaini, and A.K. Azad, *Renew. Sustain. Energy Rev.* 79, 750 (2017).
5. N. Ito, M. Iijima, K. Kimura, and S. Iguchi, *J. Power Sour.* 152, 200 (2005).
6. N. Ito, S. Aoyama, T. Masui, S. Matsumoto, H. Matsumoto, and T. Ishihara, *J. Power Sour.* 185, 922 (2008).
7. K. Katahira, H. Matsumoto, H. Iwahara, K. Koide, and T. Iwamoto, *Sens. Actuators B Chem.* 73, 130 (2001).
8. T. Yajima, K. Koide, H. Takai, N. Fukatsu, and H. Iwahara, *Solid State Ion.* 79, 333 (1995).
9. C.O. Park, J.W. Fergus, N. Miura, J. Park, and A. Choi, *Ionics* 15, 261 (2009).
10. U. Röder-Roith, F. Rettig, K. Sahnera, T. Röder, J. Janek, and R. Moos, *Solid State Ion.* 192, 101 (2011).

11. T. Sakai, K. Isa, M. Matsuka, T. Kozai, Y. Okuyama, T. Ishihara, and H. Matsumoto, *Int. J. Hydrog. Energy* 38, 6842 (2013).
12. N.S. Patki, A. Manerbino, J.D. Way, and S. Ricote, *Solid State Ion.* 317, 256 (2018).
13. T. Sakai, S. Matsushita, H. Matsumoto, S. Okada, S. Hashimoto, and T. Ishihara, *Int. J. Hydrog. Energy* 34, 56 (2009).
14. N. Danilov, A. Tarutin, J. Lyagaeva, G. Vdovin, and D. Medvedev, *J. Mater. Chem A* 6, 16341 (2018).
15. W. Deibert, M.E. Ivanova, S. Baumann, O. Guillon, and W.A. Meulenberg, *J. Membr. Sci.* 543, 79 (2017).
16. A. Vourros, V. Kyriakou, I. Garagounis, E. Vasileiou, and M. Stoukides, *Solid State Ion.* 306, 76 (2017).
17. T. Takahashi and H. Iwahara, *Rev Chim. Miner.* 17, 543 (1980).
18. J. Lyagaeva, N. Danilov, G. Vdovin, J. Bu, D. Medvedev, A. Demin, and P. Tsiakaras, *J. Mater. Chem. A* 4, 40 (2016).
19. D.A. Medvedev, J.G. Lyagaeva, E.V. Gorbova, A.K. Demin, and P. Tsiakaras, *Prog. Mater Sci.* 75, 38 (2016).
20. D. Medvedev, A. Murashkina, E. Pikalova, A. Demin, A. Podias, and P. Tsiakaras, *Prog. Mater Sci.* 60, 72 (2014).
21. J. Lu, L. Wang, L. Fan, Y. Li, L. Dai, and H. Guo, *J. Rare Earths* 26, 505 (2008).
22. Y. Okuyama, T. Kozai, T. Sakai, M. Matsuka, and H. Matsumoto, *Electrochim. Acta* 95, 54 (2013).
23. I. Animitsa, A. Iakovleva, and K. Belova, *J. Solid State Chem.* 238, 156 (2016).
24. T. Tu, B. Zhang, J. Liu, K. Wu, and K. Peng, *Electrocim. Acta* 283, 1366 (2018).
25. B. Zhang, Z. Zhong, T. Tu, K. Wu, and K. Peng, *J. Power Sour.* 412, 631 (2018).
26. L. Hakimova, A. Kasyanova, A. Farlenkov, J. Lyagaeva, D. Medvedev, A. Demin, and P. Tsiakarasa, *Ceram. Int.* 45, 209 (2019).
27. Y. Okuyama, S. Ikeda, T. Sakai, and H. Matsumoto, *Solid State Ion.* 262, 338 (2014).
28. Y. Okuyama, T. Kozai, S. Ikeda, M. Matsuka, T. Sakai, and H. Matsumoto, *Electrochim. Acta* 125, 443 (2014).
29. N.A. Shafiqa, M.S. Idris, C.A. SalmieSuhana, R.A.M. Osman, and T.Q. Tan, *Mater. Sci. Forum* 819, 117 (2015).
30. V.B. Balakireva, A.Yu. Stroeva, and V.P. Gorelov, *Russ. J. Electrochem.* 41, 535 (2005).
31. Web-site of Institute of High Temperature Electrochemistry. http://www.ihte.uran.ru/?Page_id=3106. Accessed 20 March 2019.
32. FullProf Suite. https://www.ill.eu/sites/fullprof/php/downloads.html. Accessed 20 March 2019.
33. GetData Graph Digitizer. http://getdata-graph-digitizer.com/index.php. Accessed 20 March 2019.
34. C.A. SalmieSuhana, N.S. Hazwani, N.A. Shafiqa, and W.N. ImaduddinHelmi, *Adv. Mater. Res.* 795, 513 (2013).
35. B.-X. Liu, Q. Yang, Y.-X. Guo, C. Chen, G.-L. Ma, and H.-T. Wang, *Chin. J. Inorg. Chem.* 25, 278 (2009).
36. M. Mizuno, A. Rouanet, T. Yamada, and T. Noguchi, *Yogyo-Kyokai-Shi* 84, 7 (1976).
37. J. Coutures, A. Rouanet, R. Verges, and M. Foex, *J. Solid State Chem.* 17, 172 (1976).
38. V.P. Gorelov, Z.S. Martem'yanova, and V.B. Balakireva, *Inorg. Mater.* 35, 153 (1999).
39. V.M. Goldschmidt, *Naturwissenschaften* 14, 477 (1926).
40. C. Artini, M. Pani, A. Lausi, and G.A. Costa, *J. Phys. Chem. Solids* 91, 93 (2016).
41. G.A. Tompsett, R.J. Phillips, N.M. Sammes, and A.M. Cartner, *Solid State Commun.* 108, 655 (1998).
42. A. Siaï, P. Haro-Gonzalez, K. HorchaniNaifer, and M. Ferid, *Opt. Mater.* 76, 34 (2018).
43. C. Artini, *J. Eur. Ceram. Soc.* 37, 427 (2017).
44. Y.-C. Wu and C.-R. Rao, *Ceram. Int.* 44, 19706 (2018).
45. S.L. Reis and E.N.S. Muccillo, *Ionics* 24, 1693 (2018).
46. A.V. Kuzmin, A. Yu Stroeva, M.S. Plekhanov, V.P. Gorelov, and A.S. Farlenkov, *Int. J. Hydrog. Energy* 43, 19206 (2018).
47. A.V. Kuzmin, A.S. Lesnichyova, M.S. Plekhanov, AYu Stroeva, V.A. Vorotnikov, and A.V. Ivanov, *Russ. J. Appl. Chem.* 91, 1434 (2018).
48. D.-K. Lim, H.-N. Im, S.-J. Song, and H.-I. Yoo, *Sci. Rep.* 7, 486 (2017).
49. H. Zhu, S. Ricote, C. Duan, R.P. O'Hayre, and R.J. Kee, *J. Electrochem. Soc.* 165, F845 (2018).
50. D.-K. Lim, T.-R. Lee, B. Singh, J.-Y. Park, and S.-J. Song, *J. Electrochem. Soc.* 161, F710 (2014).
51. W. Wang, D. Medvedev, and Z. Shao, *Adv. Funct. Mater.* 28, 1802592 (2018).
52. V. Besikiotis, C.S. Knee, I. Ahmed, R. Haugsrud, and T. Norby, *Solid State Ion.* 228, 1 (2012).
53. E.P. Antonova, M.V. Ananyev, A.S. Farlenkov, E.S. Tropin, A.V. Khodimchuk, and N.M. Porotnikova, *Russ. J. Electrochem.* 53, 651 (2017).